

Modeling of coupled liquid-gas-solid three-phase processes due to fluid injection

Yong-Ge Zang¹, Dong-Mei Sun^{*1}, Ping Feng¹ and Semprich Stephan²

¹ State Key Laboratory of Hydraulic Engineering Simulation and Safety,
Tianjin University, Tianjin 300072, China

² Institute of Soil Mechanics and Foundation Engineering,
Graz University of Technology, 8010 Graz, Austria

(Received July 21, 2016, Revised January 18, 2017, Accepted February 03, 2017)

Abstract. A coupled liquid-gas-solid three-phase model, linking two numerical codes (TOUGH2/EOS3 and FLAC^{3D}), was firstly established and validated by simulating an in-situ air flow test in Essen. Then the coupled model was employed to investigate responses of multiphase flow and soil skeleton deformation to compressed air or freshwater injection using the same simulation conditions in an aquifer of Tianjin, China. The simulation results show that with injecting pressurized fluids, the vertical effective stress in some area decreases owing to the pore pressure increasing, an expansion of soil skeleton appears, and land uplift occurs due to support actions from lower deformed soils. After fluids injection stops, soil deformation decreases overall due to injecting fluids dissipating. With the same applied pressure, changes in multiphase flow and geo-mechanical deformation caused by compressed air injection are relatively greater than those by freshwater injection. Furthermore, the expansion of soil skeleton induced by compressed air injection transfers upward and laterally continuously with time, while during and after freshwater injection, this expansion reaches rapidly a quasi-steady state. These differences induced by two fluids injection are mainly because air could spread upward and laterally easily for its lower density and phase state transition appears for compressed air injection.

Keywords: coupled liquid-gas-solid three-phase model; compressed air injection; freshwater injection; geo-mechanical analysis; effective stress

1. Introduction

The subsurface fluids injection has been widely used in many geo-environmental situations for various purposes, such as enhancing oil production, storing useful and valuable gas or oil, recharging aquifer systems, arresting or mitigating land subsidence, disposing of contaminants and hazardous wastes, and other applications (Selvadurai 2003, 2006, Chen *et al.* 2007, Bell *et al.* 2008, Wong and Lau 2008, Sreng *et al.* 2009, Teatini *et al.* 2011, Rutqvist 2012). For example, the injection of water-based solutions, hydrocarbons, CO₂ or N₂, is usually used to recover additional oil from depleted or water-flooded reservoirs through displacing oil with injected fluids (Rao 2001, Teatini *et al.* 2011). The injecting compressed air can be used to mitigate seawater intrusion in coastal regions (Dror *et al.* 2004). By introducing compressed air into a confined aquifer through

*Corresponding author, Ph.D., Associate Professor, E-mail: sundongmei@tju.edu.cn

boreholes in the row of air injection wells, seawater is ejected from the aquifer and the seawater circulation disappears (Sun and Semprich 2013). During the tunnel construction, using compressed air injection could also prevent groundwater inflow through excavated surface and reduce the ground surface settlement, then balance the groundwater and stabilize the tunnel face (Kramer and Semprich 1989, Chinkulkijniwat *et al.* 2014). Specifically, land subsidence, generally arising from over-pumping of groundwater and extraction of oil or gas, is usually more progressive and beyond retrieve. The effective measures to mitigate this problem are generally restricting groundwater extraction and augmenting groundwater recharge, and especially in coastal regions, seawater can also be injected to arrest land subsidence (Teatini *et al.* 2000, Sreng *et al.* 2009).

Actually, these behaviors of pressurized fluids injection all involve an interaction between geo-mechanical and multiphase fluids flow processes, and could alter the stress state and seepage field in the soil skeleton and porous media (Selvadurai 2009, Rutqvist *et al.* 2010, Teatini *et al.* 2011, Kim and Selvadurai 2015). A coupled geo-mechanics-multiphase flow model could therefore produce a more realistic result. Three basic algorithms: fully coupling, one-way coupling and loosely coupling, are available for coupling multiphase porous flow and geo-mechanics (Minkoff *et al.* 2003). In a fully coupling methodology, a single set of equations incorporating all the relevant physics of multiphase flow and geo-mechanical deformation (generally a large system of nonlinear coupled partial differential equations), i.e., the multiphase flow equations contain terms for deformation and vice versa, are solved simultaneously at every time step. This methodology can provide a stable and accurate solution if the mathematical problem is well posed, and has been used in several engineering problems of coupled multiphase flow and geo-mechanics (Pao *et al.* 2001, Gutierrez and Lewis 2002, Pao and Lewis 2002, Lewis *et al.* 2003, Jeannin *et al.* 2007). But it requires a unified flow-mechanics simulator, a unified grid, huge matrices, and large memory requirements, leading to computationally expensive for realistic fields (Armero and Simo 1992, Settari and Mourits 1998, Settari and Walters 2001, Thomas *et al.* 2003, Vijalapura *et al.* 2005, Jha and Juanes 2007). In a one-way coupling methodology, the multiphase flow equation and geo-mechanics equation are solved independently at the same time-step, and the output from one simulator is passed to another one in only one direction. This algorithm is relatively simple to implement but actually is not fully representative of the tightly coupled flow and geo-mechanics (Kim *et al.* 2012). A loosely coupling methodology also allows for using separate simulators and grids for each sub-problem, producing smaller systems of equations to be solved than the fully coupling methods (Felippa and Park 1980), and it is highly attractive for handling the multiphase flow and geomechanical processes (Rutqvist *et al.* 2002, Settari and Sen 2007). In this method, the two existing simulators with respect to the multiphase flow and geo-mechanics are solved sequentially, and are communicated through a well-defined interface to transmit reciprocally the relevant variables at the specified time-step (Rutqvist *et al.* 2002, Minkoff *et al.* 2003, Samier *et al.* 2008). Moreover, its produced results are close to that of the fully coupling method if a tight tolerance and small time-step are used (Dean *et al.* 2006).

Therefore in this study, a loosely coupled methodology (Rutqvist *et al.* 2002, Rutqvist and Tsang 2003), in which TOUGH2 is used for solving multiphase multi-component flow equations (Pruess *et al.* 1999), whereas FLAC^{3D} is used for solving geo-mechanical stress-strain equations (ITASCA 2002), was engaged to simulate the liquid-gas-solid three-phase coupling processes induced by compressed air or freshwater injection in an aquifer of Tanggu District, Tianjin, China. This coupled simulator has been widely applied in many energy-development and environment-management events, such as nuclear waste disposal, CO₂ sequestration, geothermal energy extraction, naturally occurring CO₂ upwelling with surface deformations, and gas production from

hydrate-bearing sediments (Rutqvist and Moridis 2007, Rutqvist 2008, Cappa *et al.* 2009, Rutqvist *et al.* 2009, 2010, Tsang *et al.* 2008). As well, the difference in distribution features of seepages and stress fields between these two fluids injection was compared, and the reason for this difference was explained.

2. Liquid-gas-solid three-phase coupling procedures

TOUGH2/EOS3 is a module in TOUGH2 for non-isothermal water-air two-phase flow in three-dimensional unsaturated-saturated porous and fractured media, in which the transformation and dissolution processes occurring between the liquid phase and gas phase are explained by mass balance equations. FLAC^{3D} is a three-dimensional, explicit finite-difference computer code for solving geo-mechanical stress-strain equations. In the coupled liquid-gas-solid three-phase process, the seepage process affects the stresses field through changing the pore pressure and the effective stresses, whereas the stresses field affects the seepages through changing the porosity, the capillary pressure and the intrinsic permeability.

2.1 Update of geo-mechanical variables

In the coupled procedure, the pore water pressure p_l , the pore air pressure p_g , and the liquid saturation S_l provided by TOUGH2/EOS3 (the pore pressures are referred to the local atmospheric pressure, and the same below) are sent to FLAC^{3D} to calculate the average pore pressure p (Rutqvist *et al.* 2002)

$$p = S_l p_l + (1 - S_l) p_g \quad (1)$$

Then FLAC^{3D} internally calculates the stress, the strain, the displacement and the effective stress σ'_{ij} ($\sigma'_{ij} = \sigma_{ij} - p\delta_{ij}$, where σ_{ij} is the total stress, and δ_{ij} is Kronecker function (for $i = j$, $\delta_{ij} = 1$; for $i \neq j$, $\delta_{ij} = 0$)). The change in porosity $d\phi$ induced by the soil deformation can be expressed as (Coussy 1995, Bary 2002)

$$d\phi = (1 - \phi_0)\varepsilon_v \quad (2)$$

where ϕ_0 is the initial porosity at zero stress, and ε_v is the volumetric strain increment. Here it is assumed that the deformation of solid grain is much less than that of soil skeleton, and can be negligible.

2.2 Update of hydraulic variables

The geo-mechanically induced $d\phi$ has an immediate effect on the fluid flow behavior, including the intrinsic permeability and the capillary pressure. The intrinsic permeability is estimated by employing appropriate scaling equations, and here Kozeny-Carman Equation (Chapuis and Aubertin 2003) is applied.

$$K = K_0 \left(\frac{\phi}{\phi_0} \right)^3 \left(\frac{1 - \phi_0}{1 - \phi} \right)^2 \quad (3)$$

Where K is the corrected intrinsic permeability, K_0 is the initial intrinsic permeability, and ϕ is the current porosity.

The capillary pressure is scaled with the current intrinsic permeability and current porosity according to a function by Leverett (1941).

$$p_{cl} = p_c \frac{\sqrt{K_0 / \phi_0}}{\sqrt{K / \phi}} \quad (4)$$

Where p_{cl} is the corrected capillary pressure, and p_c is the calculated capillary pressure dependent on the liquid saturation.

2.3 Coupling procedures

The coupling method between TOUGH2/EOS3 and FLAC^{3D} is typically developed according to the procedure in Fig. 1. Some input data files for TOUGH2/EOS3 and FLAC^{3D} must be prepared before the coupling process, such as soil properties, mesh, boundary conditions, and initial conditions. Then TOUGH2/EOS3 is executed for a sufficient simulation time to obtain an initial steady condition, and FLAC^{3D} is also operated under gravitational loads to establish initial equilibrium stress gradients and outputs the initial porosity ϕ_0 of each element. Hereafter, the coupling process of TOUGH2/EOS3-FLAC^{3D} starts. The initial porosity ϕ_0 from FLAC^{3D} element is mapped to TOUGH2/EOS3 element, which is used to update the intrinsic permeability according to Eq.(3). TOUGH2/EOS3 is firstly executed for the first time-step, and the capillary pressure is corrected by Eq.(4). When convergence is reached at the end of this time-step, the pore water pressure p_l , the pore air pressure p_g , and the liquid saturation S_l of each element in TOUGH2/EOS3 are obtained and are mapped to FLAC^{3D} nodes by weighted distance interpolation. Then FLAC^{3D} runs under loads of average pore pressure at each node (which can be calculated by Eq. (1)), until reaching an equilibrium state. At this point, the change in porosity at FLAC^{3D} element can be calculated according to the strain increment (by Eq. (2)). Afterwards, the updated porosity at FLAC^{3D} element is sent back to the TOUGH2/EOS3 element by interpolation. Utilizing the updated porosity, the intrinsic permeability is updated again according to Eq. (3), and TOUGH2/EOS3 is executed for the next time-step. And then the above coupling processes are repeated until reaching the specified simulation time (Sum-time).

3. Validation of coupled liquid-gas-solid three-phase model

The coupled liquid-gas-solid three-phase model was validated by simulating an in-situ air flow test in Essen, which was carried out to explore the behavior of the outcropping types of Essen soils before the subway construction using compressed air technique in Essen, Germany (Kramer and Semprich 1989). Fig. 2 shows a schematic diagram of the experimental set-up for the in-situ air flow test. The soil profile in Essen consists of four distinct layers: a fill layer, a thick silt layer, a thin highly permeable sand layer and a thick layer of marl which is rather weathered in the upper region and presents pronounced joints. The groundwater table is about 4.75 m below the ground surface.

In the experiment under consideration here, the applied air pressure Δp was 160 kPa over 27 h. Compressed air could be introduced into the ground through the borehole of 1.5 m diameter in the injection well. A thin steel pipe can be installed inside the borehole, the lower part of the pipe (18.0 m to 21.0 m below the ground surface) being perforated and the top of the pipe being connected to an air compressor (which was used to control the air pressure) (Kramer and Semprich

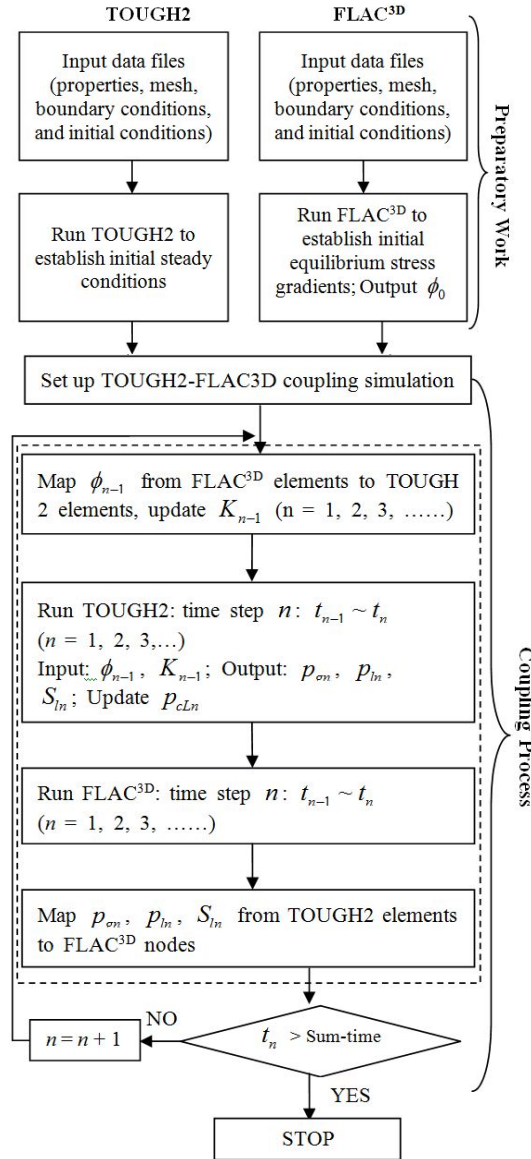


Fig. 1 Flow chart for loosely coupling algorithm

1989). The rate of injection air was monitored by flow meter during the experiment. Several piezometers were installed near the borehole to measure the variations of pore pressure at different depths and at different distances from the borehole. The ground surface displacement was measured by geodetic leveling installed at different distances from the borehole. More details of the in-situ air flow test can be found in Kramer and Semprich (1989).

Taking advantage of the axial symmetry of this problem, only one fourth of the domain was simulated. The model domain was 100 m long in both the transverse direction (X) and the longitudinal direction (Y), and was 25 m high in the vertical direction (Z). In this study, the mesh generation in TOUGH2/EOS3 was the same as that in FLAC^{3D}, consisting of 18259 hexahedron

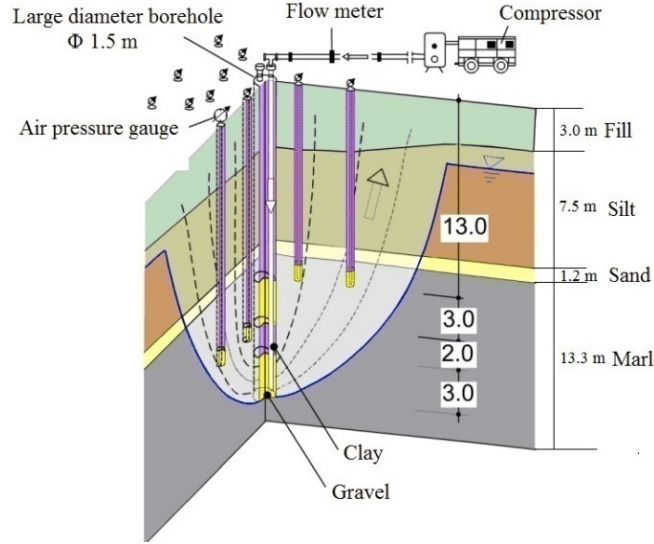


Fig. 2 In-situ air flow test in Essen (Kramer and Semprich, 1989)

elements and 20480 nodes, and is shown in Fig. 3. The mesh in the vertical direction was divided to take into account the soil layers, the groundwater table and the air injection region. While the mesh size in the horizontal directions was quite fine near the borehole and expanded with the distance from the borehole. In this numerical model, the capillary pressure p_c , the relative liquid permeability k_{rl} and the relative gas permeability k_{rg} dependent on the liquid saturation were described by the van Genuchten model (later called the VG model), as described as Eq. (5) (Van Genuchten 1980), and the van Genuchten-Mualem model (later called the VG-M model), as described as Eqs. (6)-(7) (Mualem 1976, Van Genuchten 1980), respectively.

$$p_c = -p_0 \left[(S^*)^{-1/\lambda} - 1 \right]^{1-\lambda} \quad (-p_{\max} \leq p_c \leq 0) \quad (5)$$

where p_0 is the air entry pressure, λ is a model parameter associated with the degree of soil uniformity, S^* is the effective liquid saturation, $S^* = (S_l - S_{lr}) / (S_{ls} - S_{lr})$, S_l is the liquid saturation, S_{lr} is the residual liquid saturation, and S_{ls} is the saturated liquid saturation.

$$k_{rl} = \begin{cases} \sqrt{S^*} \left[1 - \left(1 - (S^*)^{1/\lambda} \right)^\lambda \right]^2 & (S_l < S_{ls}) \\ 1 & (S_l \geq S_{ls}) \end{cases} \quad (6)$$

$$k_{rg} = \begin{cases} 1 - k_{rl} & (S_{gr} = 0) \\ (1 - \hat{S})^2 (1 - \hat{S}^2) & (S_{gr} > 0) \end{cases} \quad (7)$$

where $\hat{S} = (S_l - S_{lr}) / (1 - S_{lr} - S_{gr})$, and S_{gr} is the residual gas saturation.

The hydraulic and geo-mechanical parameters for four soil layers in Essen, taken from Öttl (2003), are shown in Table 1. It is noted that the lower part of the silt layer presents a weaker

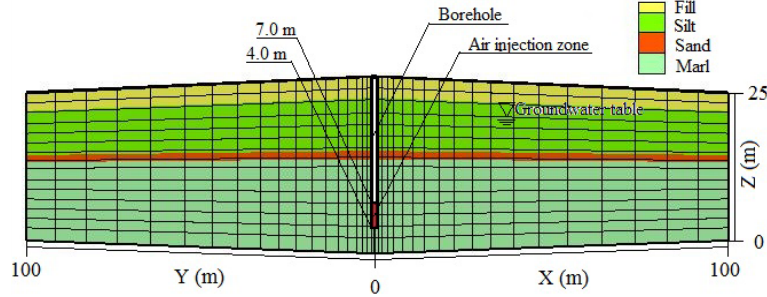

 Fig. 3 The meshes in the model of TOUGH2/EOS3 and FLAC^{3D}

Table 1 Material parameters for four soil layers in Essen

Soil texture	ρ_s , (g/cm ³)	ϕ	K , (10 ⁻¹² m ²)	p_0 , (kN/m ²)	S_{lr}
Fill	2.72	0.36	4.95	4.0	0.2
Silt	2.90	0.42	0.495	30.0	0.2
Sand	2.72	0.36	9.90	4.0	0.05
Marl	2.79	0.33	2.48	12.0	0.15
Soil texture	S_{ls}	S_{gr}	λ	E , (Mpa)	ν
Fill	1.0	0.01	0.8	20	0.33
Silt	1.0	0.01	0.5	12.47 (9.24)	0.35 (0.37)
Sand	1.0	0.01	0.65	21.22	0.32
Marl	1.0	0.01	0.6	14.33	0.40

stiffness and the stiffness properties in this region was written in parentheses in Table 1. In addition, the liner elastic behaviour was assumed for the whole domain. All processes involved in the numerical simulation were assumed to occur isothermally at 10°C.

In TOUGH2/EOS3, the primary variables are P_β (the pressure of β phase (the liquid phase (l) or gas phase (g))), X_g^a (the air-mass fraction in the β phase), and T (temperature) for single-phase conditions, and P_g , $S_g + 10$ (the gas saturation plus 10) and T (temperature) for two-phase conditions. The atmospheric boundary conditions, $P_g = p_{atm}$ (p_{atm} was the atmospheric pressure and was equal to 1.1013×10^5 pa), $X_g^a = 0.999$, and $T = 10^\circ\text{C}$, were applied at the ground surface. The Dirichlet boundary conditions, $P_l = p_{atm} + \rho_w g(20.25 - Z)$, $X_l^a = 1.0 \times 10^{-10}$, and $T = 10^\circ\text{C}$, where the water density ρ_w was 1000 kg/m^3 , and the gravitational acceleration g was 9.81 m/s^2 , and Z was the elevation of model domain, were applied at the bottom of domain. No flow boundaries were considered at the other boundaries. The initial steady condition was obtained by running TOUGH2/EOS3 with the above boundary conditions and the initial liquid-saturated condition for a sufficient simulation time until reaching a steady state.

In FLAC^{3D}, the surface of domain was specified as a free deformed boundary, whereas no deformation in the bottom of domain was allowed, i.e., $u_h = 0$ and $u_v = 0$, where u_h was the horizontal displacement, and u_v was the vertical displacement. The roller displacement boundary ($u_h = 0$) was prescribed at all the lateral boundaries. Under gravitational loads, the initial steady conditions in TOUGH2/EOS3 were sent to FLAC^{3D} to calculate the initial equilibrium stress

distributions that were used as the initial conditions for the FLAC^{3D} model. This calculation was the first couple between the TOUGH2/EOS3 model and the FLAC^{3D} model.

Then using the reproducing initial-steady conditions of the TOUGH2/EOS3 model and FLAC^{3D} model as the initial condition of these two models respectively, the soil elements in the air injection region in the TOUGH2/EOS3 model were replaced by the air elements, whose primary variables were $P_g = p_{atm} + \Delta p$, $X_g^a = 0.999$ and $T = 10^\circ\text{C}$, and the above borehole elements were removed. Then the coupled hydraulic-mechanical process, considering the interactions between the liquid phase, gas phase and the solid phase, were repeated until the simulation time of 27 h was reached.

Fig. 4 shows the distributions of simulated pore pressure at 27 h after compressed air injection. Due to the compressed air injection, the pore pressure increased greatly near the injection zone, and decreased gradually with the distance from the borehole. The pore pressures at four observed points A, B, C and D measured by the piezometers were 27 kPa, 70 kPa, 95 kPa and 90 kPa, respectively. As can be seen in Fig. 4, there was a good agreement between the measured and simulated results.

The simulated and measured surface displacements at different distances from the borehole after applying air pressure of 27 h are shown in Fig. 5. The surface heave appeared and the maximum simulated vertical displacement of 3.8 mm occurred near the borehole. Additionally, the surface displacement decreased with the distance from the borehole, and remained substantially unchanged as the distance from the borehole was about 60 m. Considering that the soil layers were assumed to be homogeneous and isotropic in the numerical simulation, whereas the soil

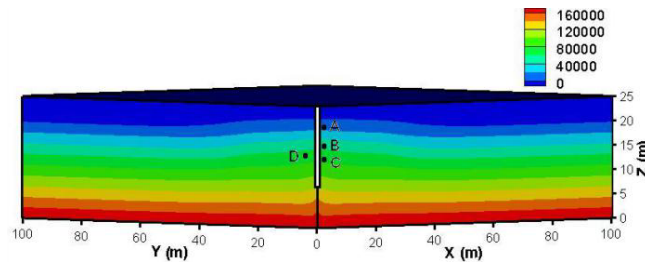


Fig. 4 The distributions of simulated pore pressure after applying air injection for 27 hours (unit: Pa)

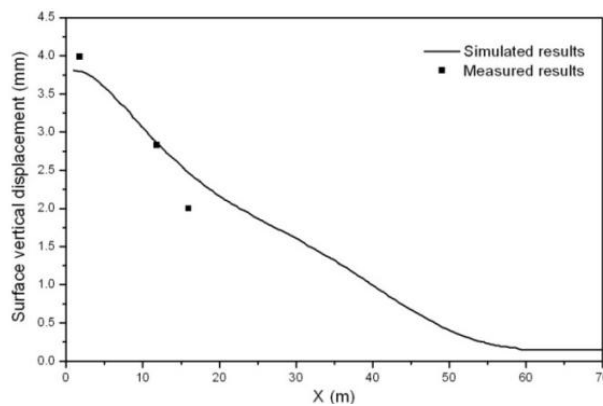


Fig. 5 The surface displacement after applying air injection for 27 hours

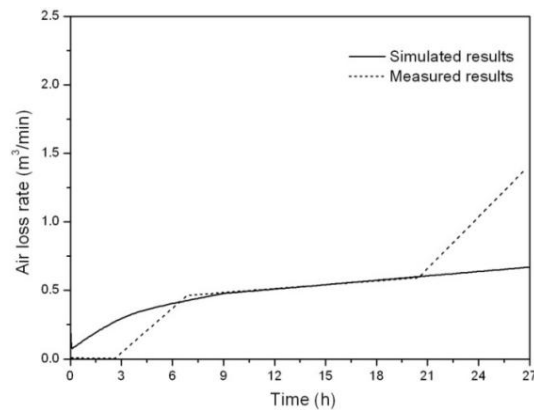


Fig. 6 The temporal evolution of air injection rate during compressed air injection

permeabilities were highly anisotropy in both the horizontal and vertical direction (Kramer and Semprich 1989), the difference between the measured and simulated results could be acceptable.

Fig. 6 compares the time evolution of the measured and simulated air loss rates during the air injection process. Clearly, the simulated air loss rate increased greatly at first, then varied slowly and reached nearly a steady value. It was substantially the same as the measured result during the middle period, whereas there were great differences between them at the initial and final stage. In the field test, the applied air pressure was increased stepwise to 160 kPa by the compressor. Before the air pressure reached 160 kPa, the matric suction in marl layer could not surpass the air entry value of marl, and no air penetrated into the soil. So the air loss rate was nearly zero before 3 h. When the air pressure reached 160 kPa, the compressed air entered into the soil, and the air loss rate increased rapidly. However, in the numerical simulation, the applied air pressure was prescribed to be 160 kPa from the beginning, so the differences between the measured and simulated results were caused at the initial stage (Chinkulkijniwat 2005, Chinkulkijniwat *et al.* 2014). At about 21 h after the air injection, owing to the high permeability in sand layer and the anisotropy in both the horizontal and vertical direction (Kramer and Semprich 1989), the compressed air flowed horizontally along the sand layer in the field test. Additionally, there existed fractured media at the depth of 13 m according to the site survey, so the air loss increased significantly when the air flowed to the fracture media (Chinkulkijniwat 2005, Chinkulkijniwat *et al.* 2014). But a continuous and isotropic porous media was assumed in the numerical model. Therefore, the difference between the measured and simulated results could be explainable.

4. Model study

4.1 Geometry description and numerical method

This study, taking the aquifer of Tanggu District, Tianjin, China for example, mainly focused on the geo-mechanical and water-air two-phase flow processes separately induced by the compressed air injection and freshwater injection. According to the exploration data, the strata above 60 m in this region belongs to Quaternary Holocene and Late Pleistocene, and can be simply divided into four distinct layers: a silty clay layer, a mucky clay layer, a clay layer and a silty sand layer, as is shown in Fig. 7(a). The groundwater table is located in the silty clay layer

and is about 8.5 m below the ground surface. Compressed air or freshwater could be introduced into the ground through the borehole of 0.5 m diameter, and the screened part was 43.0 m to 51.0 m below the ground surface.

In this numerical simulation, one fourth of the domain was simulated for the axial symmetry of this problem. The model domain was set to be 200 m \times 200 m \times 60 m. As shown in Fig. 7(b), the injection well was located at X = Y = 0 and the elevation of screened part was 9 m to 17 m. The mesh generation in TOUGH2/EOS3 was the same as that in FLAC^{3D}, consisting of 31744 hexahedron elements and 34848 nodes. The capillary pressure and the relative permeability dependent on the liquid saturation were also described by the VG model (Van Genuchten, 1980) and the VG-M model (Mualem 1976, Van Genuchten 1980), respectively. The hydraulic and geo-mechanical parameters of four soils layers are listed in Table 2, in which, the unsaturated hydraulic parameters were determined by referencing the description by Van Genuchten *et al.* (1991) based on the soil layer properties and their permeabilities, and the geo-mechanical parameters were from quick direct shear test. The four soil layers were assumed to be normal consolidation soils.

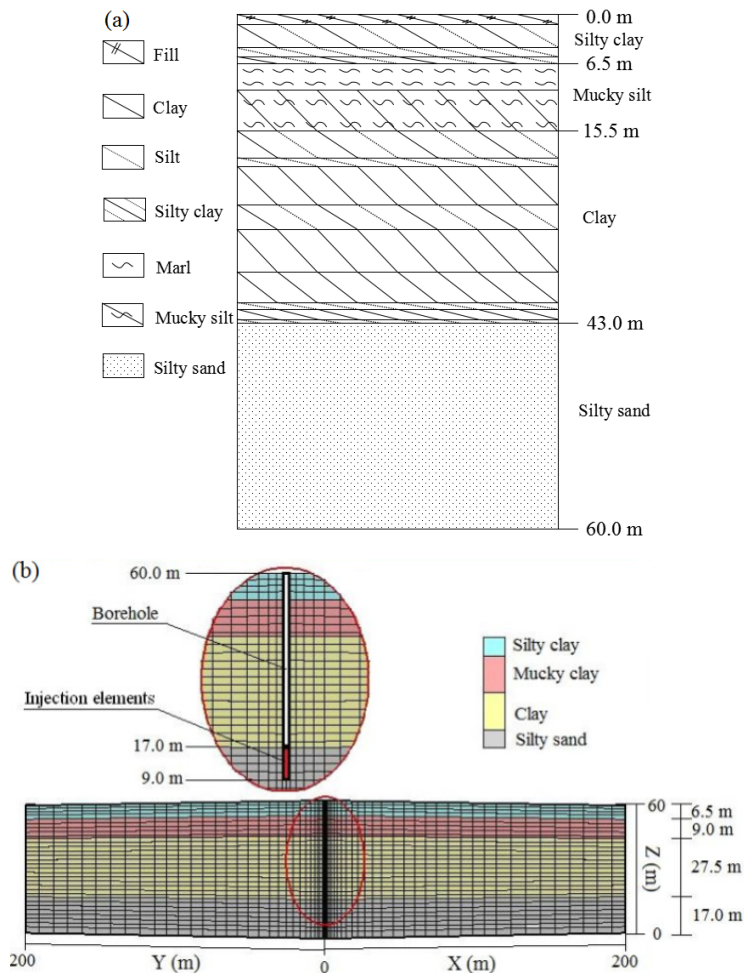


Fig. 7 (a) Geological profile of the study area; and (b) the meshes in the models of TOUGH2/EOS3 and FLAC^{3D}

Table 2 Hydraulic and geo-mechanical parameters of four soil layers in the numerical simulation

Soil texture	ρ_{ds} (g/cm ³)	ϕ	K , (10 ⁻¹³ m ²)	p_{0s} (kN/m ²)	S_{lr}
Silty clay	1.61	0.41	1.54	4.91	0.14
Mucky clay	1.31	0.52	0.77	5.16	0.21
Clay	1.54	0.44	3.09	1.66	0.22
Silty sand	1.81	0.33	37.03	0.79	0.13
Soil texture	S_{ls}	S_{gr}	λ	E , (Mpa)	ν
Silty clay	0.93	0.07	0.29	6.17	0.43
Mucky clay	0.88	0.12	0.24	3.08	0.46
Clay	0.87	0.13	0.32	5.04	0.43
Silty sand	0.93	0.07	0.56	17.76	0.31

Additionally, this study mainly focused on the difference in distribution features of geo-mechanical and water-air two-phase flow processes induced by two different fluids injection, so the problem was simplified to be liner elastic for the whole domain and isothermally at 10°C for all processes.

The settings of boundary and initial conditions in the TOUGH2/EOS3 model and FLAC^{3D} model in this numerical simulation were the same as that used in the case of in-situ air flow test in Essen. The only difference between them was the settings of elements in the injection zone. The maximum pore water pressure in the injection zone at the initial-steady state was about 408 kPa in this case. The applied air or freshwater pressure in the injection zone should be equal or greater than the maximum pore water pressure in this region, so that the air or freshwater can permeate into the soil. So the applied air or freshwater pressure Δp was set to be 420 kPa, and the whole simulation time was 90 days (10 days for fluids injection, and 80 days for fluids injection stopping), to analyze the effects of air or freshwater injection on the seepage and stress fields in the aquifer, as well the surface displacement. During compressed air injection, the injection elements (in Fig. 7(b)) in the TOUGH2/EOS3 model were replaced by the air elements, whose primary variables in the TOUGH2/EOS3 model were $P_g = p_{atm} + \Delta p$, $X_g^a = 0.999$ and $T = 10^\circ\text{C}$. During freshwater injection, the injection elements was replaced by the liquid elements, whose primary variables were $P_l = p_{atm} + \Delta p$, $X_l^a = 1.0 \times 10^{-10}$, and $T = 10^\circ\text{C}$. Specially, the borehole elements above the injection zone were also removed.

4.2 Analysis and discussion of the simulation results

4.2.1 Compressed air injection

The distributions of pore air pressure and airflow at 10.0 days are shown in Fig. 8(a). It was expected that the injected air flowed toward the zone where the groundwater pressure was lower than the applied pressure due to the pressure gradient, and the pore air pressure near and above the injection zone increased. This influence range reached about 100 m horizontally. Moreover, the changes in pore air pressure became smaller with the distance from the injection zone increasing. Especially, the pore air pressure still remained its initial values near the ground surface. The pore water pressure varied in a similar way to the pore air pressure, and also increased in the corresponding zone (not shown). Correspondingly, due to the compressed air permeating into the

soil, the soil layer near the injection zone became unsaturated at 10.0 days (in Fig. 8(b)). However, owing to the relatively high permeability in the silty sand layer, compressed air mainly flowed horizontally along the silty sand layer (in Fig. 8(a)), and the unsaturated zone was mostly concentrated in this region. Whereas the unsaturated zone in the above clay layer was small as a result of its lower permeability and higher air entry value.

Fig. 8(c) shows the distributions of pore air pressure and airflow at 30.0 days (20.0 days after compressed air injection stopped). As can be seen, after compressed air injection stopped, the air still flowed upwardly and laterally due to the density difference and the pressure gradient, but the

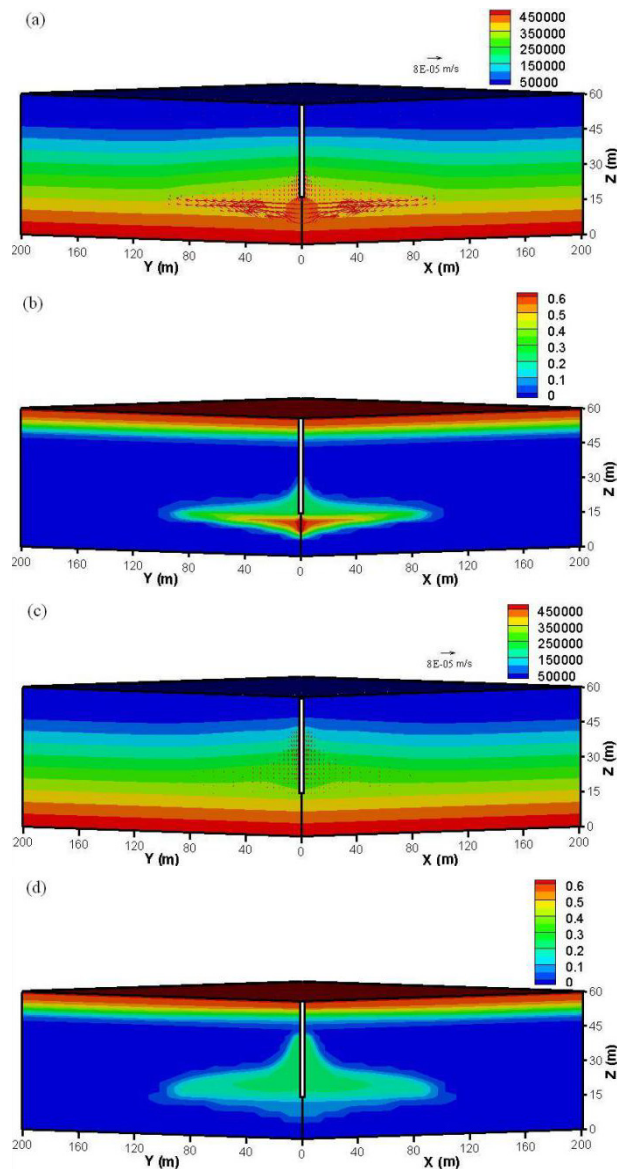


Fig. 8 The distributions of: (a) pore air pressure (unit: Pa) and airflow; and (b) gas saturation at 10.0 days; (c) pore air pressure (unit: Pa) and airflow; and (d) gas saturation at 30.0 days

magnitude of air velocity was much smaller than that at 10.0 days. The pore air pressure near the injection zone tended to decrease to its initial value, while the pore air pressure above the injection zone was greater than its initial value due to the upward airflow. Similarly, the zone where the air flowed became unsaturated (in Fig. 8(d)). Moreover, the liquid saturation near the injection zone increased because the adjacent groundwater flowed gradually to this region.

Fig. 9 shows the distributions of vertical effective stress at 10.0 days and 30.0 days. Since the total stress acting on the soil layers remained almost unchanged (the mass of injecting air was very small in relative to the weight of whole soil layers) and the stress overtaken by the fluids in soil voids increased (in Figs. 8(a) and (c)), the stress overtaken by the solid skeleton decreased, i.e., the effective stress in the corresponding zones decreased to be smaller than its initial steady value. Additionally, the distributions of decrease in the vertical effective stress were similar to those of increase in the pore pressure at the corresponding time. This release of vertical effective stress could cause an expansion of soil skeleton in the corresponding zone. The magnitude of porosity in the corresponding zone therefore increased (in Figs. 10(a)-(c)). During compressed air injection (in Figs. 10(a)-(b)), with air flowing to the surroundings, the expansion of soil skeleton transferred upward and laterally continuously with time, and the maximum value of porosity increment occurred near the borehole. After compressed air injection stopped (in Fig. 10(c)), because the vertical effective stress above the injection zone decreased (in Fig. 9(b)), the region where the porosity increased was mainly concentrated above the injection zone. Meanwhile, comparing to the distributions of porosity increment at 10.0 days, the location of the maximum value of porosity increment moved upwardly, but both the magnitude and scope of porosity increment decreased at 30.0 days.

With compressed air being injected into the soil layers, the porosity near the ground surface remained unchanged (in Fig. 10), so the land uplift was caused by the support action from the lower deformed soils. The distributions of surface vertical displacement at 10.0 days are shown in Fig. 11(a). A positive value represented that the displacement of the soil was upward (the same

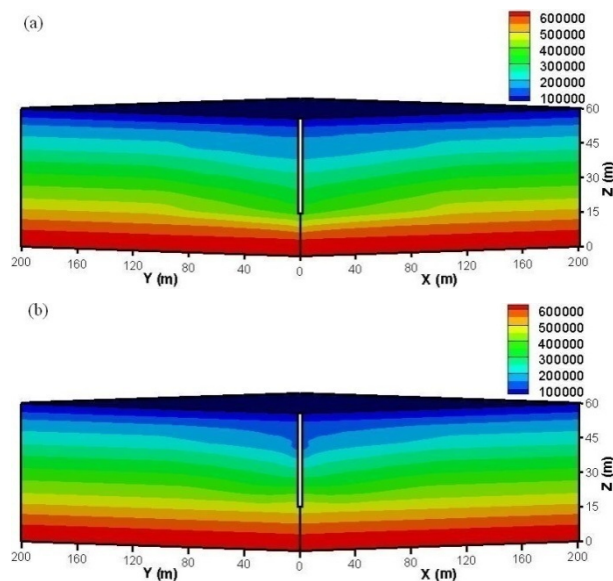


Fig. 9 The distributions of vertical effective stress at: (a) 10.0 days; and (b) 30.0 days (unit: Pa)

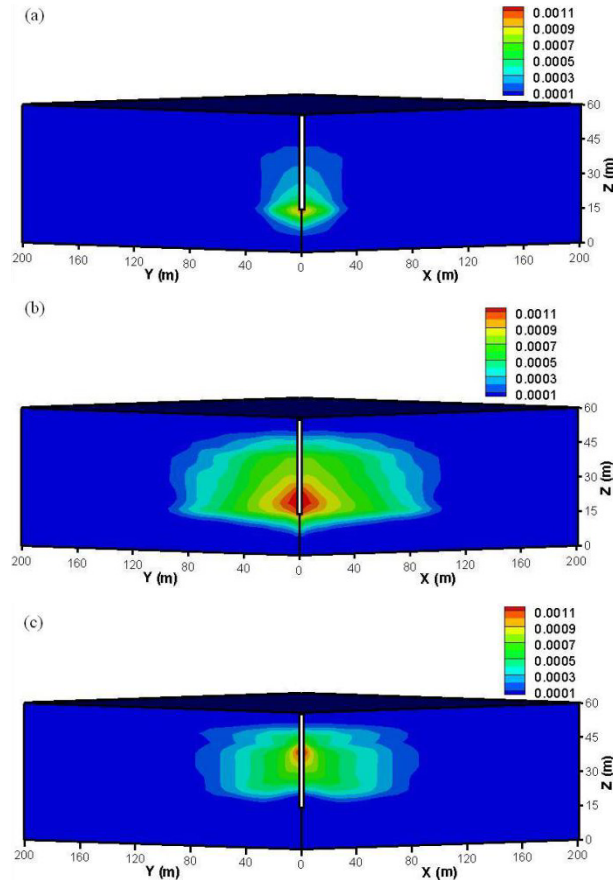


Fig. 10 The distributions of porosity increment at: (a) 1.0 day; (b) 10.0 days; and (c) 30.0 days

below). The maximum surface vertical displacement appeared near the borehole, and reached about 35 mm. But its value decreased gradually with the increasing distance from the borehole. This phenomenon was related to the distribution features of porosity increment in the lower deformed soils (in Fig. 10(b)). Fig. 11(b) shows how the surface displacement profile at $y = 0$ m changes at different times after applying compressed air injection. Clearly, during the compressed air injection, with the soil skeleton near and above the injection zone expanding continuously, the surface vertical displacement increased gradually with respect to the proceeding time. After the air injection stopped, due to the injecting air dissipating, this surface displacement decreased from 10.0 days to 14.0 days. While from 14.0 days to 20.0 days, due to the upward migration of soil skeleton expansion, the surface vertical displacement increased again, but the magnitude of the surface vertical displacement at 20.0 days was still smaller than that at 10.0 days.

The mass flux of fluids (unit: kg/s) injected into the aquifer was calculated by the numerical model, the air density under normal conditions of atmospheric pressure and 10°C was determined by the ideal gas law and the freshwater density was 1000 kg/m^3 . So the volume flux of fluids (m^3/min) injected into the aquifer could be calculated. Fig. 12 shows the time evolution of air injection rate through the injection section during compressed air injection. This rate increased gradually at first, and then changed slowly, which suggested that in the later period of air injection,

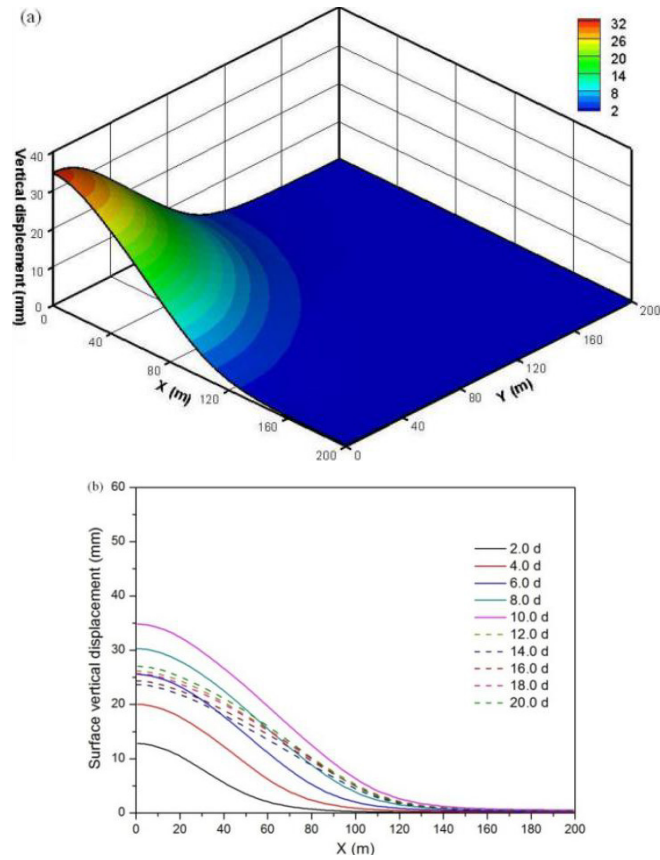


Fig. 11 (a) A 3D plot of surface vertical displacement at 10.0 days (unit: mm); and (b) surface vertical displacement profiles at $y = 0$ m at different times after applying air injection

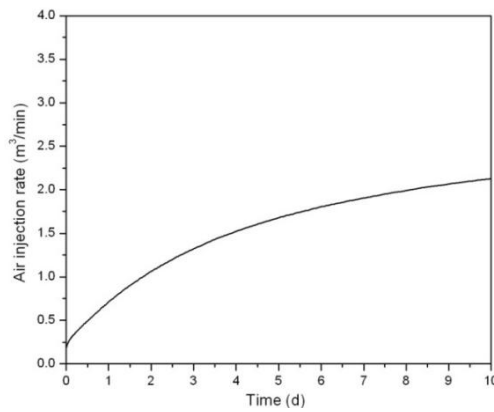


Fig. 12 The temporal evolution of air injection rate during compressed air injection

the liquid saturation, the relative gas permeability and the pressure gradient near the air injection zone changed relatively small.

4.2.2 Freshwater injection

The distributions of pore water pressure and water flow at 10.0 days and 30.0 days are shown in Fig. 13. It was expected that the regions below the groundwater table always remained liquid-saturated. At 10.0 days, near the injection zone, the pore water pressure increased as well and water flowed to the surroundings due to the pressure gradient. But both the magnitude and scope of the rise in pore water pressure were very small. This was because that the density of injected freshwater was considerably close to that of groundwater, and it was difficult for freshwater to

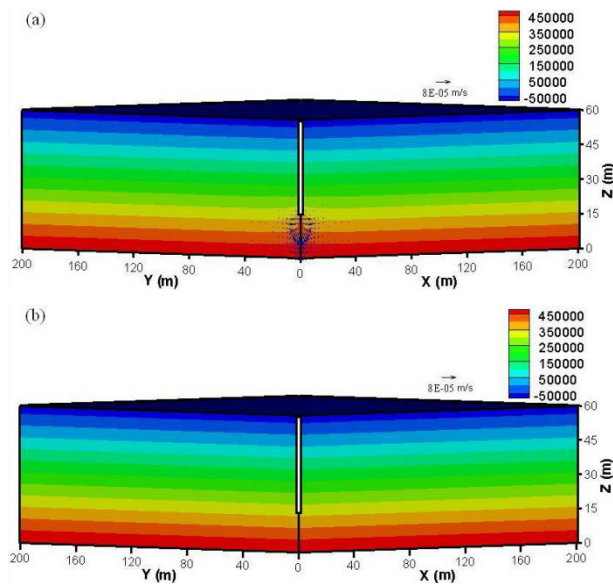


Fig. 13 The distributions of pore water pressure (unit: Pa) and water flow at: (a) 10.0 days; and (b) 30.0 days

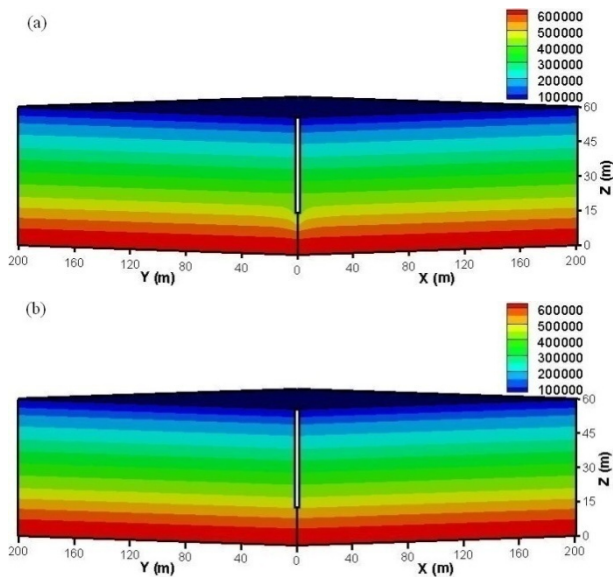


Fig. 14 The distributions of vertical effective stress at: (a) 10.0 days; and (b) 30.0 days (unit: Pa)

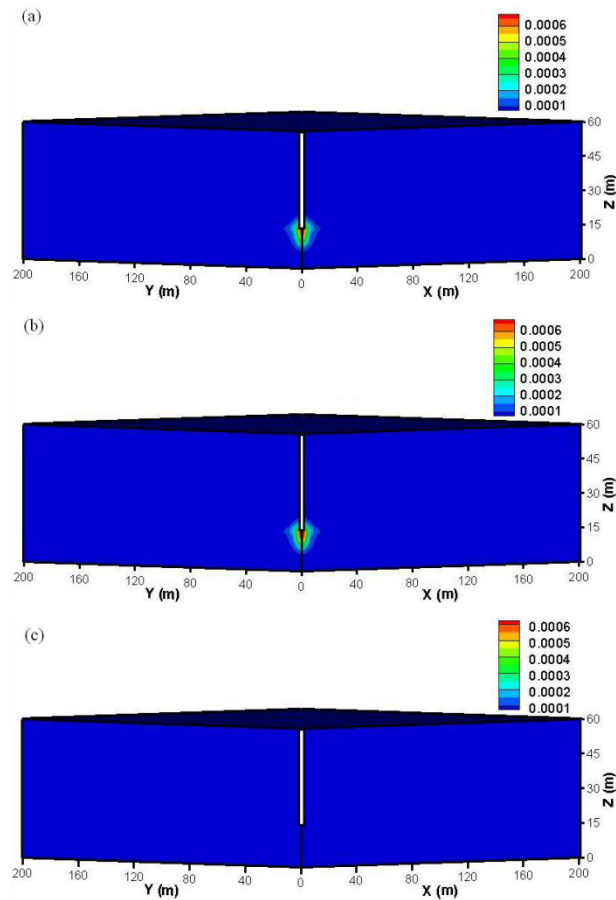


Fig. 15 The distributions of porosity increment at: (a) 1.0 day; (b) 10.0 days; and (c) 30.0 days

flow into the aquifer. At 30.0 days, the water flow in the aquifer disappeared, and the pore water pressure recovered to its initial values. Correspondingly, the decrease in vertical effective stress and the porosity increment in the corresponding zone at 10.0 days were also small (in Figs. 14(a) and 15(b)), and both these two variables recovered to its initial values, respectively, at 30 days (in Figs. 14(b) and 15(c)). In particular, the distribution of porosity increment at 1.0 day (in Fig. 15(a)) was almost the same as that at 10.0 days (in Fig. 15(b)), meaning that the soil deformation during freshwater injection reached rapidly a quasi-steady state.

Fig. 16(a) shows the distributions of surface vertical displacement at 10.0 days. Because the porosity remained unchanged near the ground surface (in Fig. 15), the surface vertical displacement was also caused by the support action from the lower deformed soils. The surface vertical displacement at 10.0 days induced by freshwater injection varied in a similar way to that induced by compressed air injection (in Fig. 11(a)), but its magnitude was much smaller and the maximum value only reached 0.45 mm. Fig. 16(b) shows the surface vertical displacement profiles at $y = 0$ m at different times after applying freshwater injection. During freshwater injection, because the porosity increment in soil interior reached rapidly a quasi-steady state, the surface vertical displacement also increased a little with the proceeding time. After the freshwater injection stopped, this displacement decreased quickly to a very small value and remained

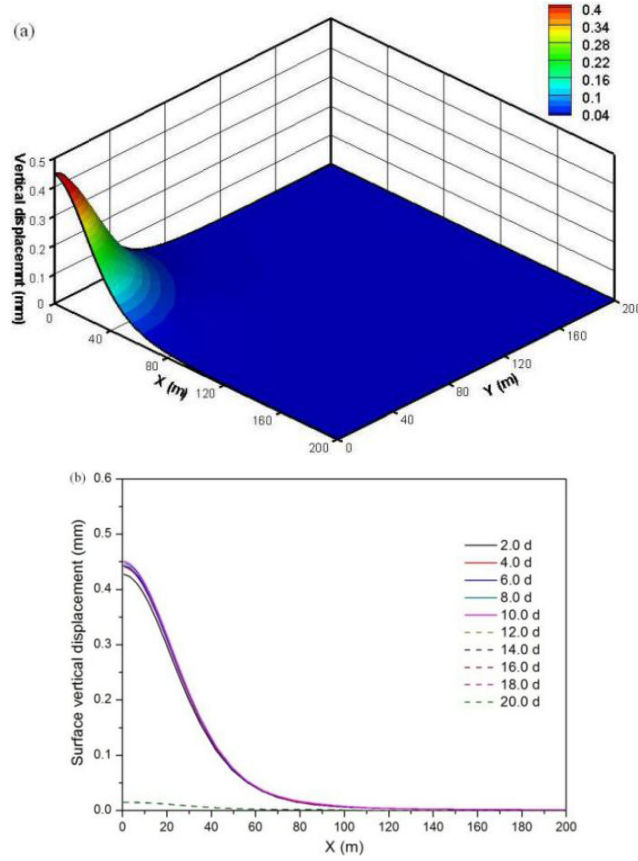


Fig. 16 (a) A 3D plot of surface vertical displacement at 10.0 days (unit: mm); and (b) surface vertical displacement profiles at $y = 0$ m at different times after applying freshwater injection

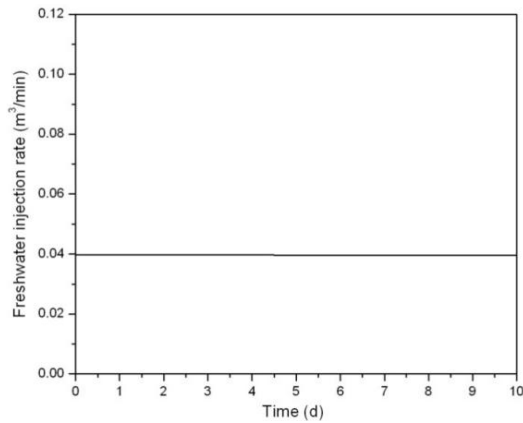


Fig. 17 The temporal evolution of freshwater injection rate during freshwater injection

unchanged, meaning that a quasi-steady state was also obtained rapidly after the freshwater injection stopped.

Fig. 17 shows how the freshwater injection rate through the injection section changes with time. During freshwater injection, the hydraulic conductivity near the injection zone kept unchanged due to the liquid-saturated state, and the pore pressure increased a little near the injection zone (in Fig. 13(a)). Therefore, the freshwater injection rate almost retained a constant value of about $0.04 \text{ m}^3/\text{min}$ during freshwater injection. This constant injection rate also meant that a quasi-steady state was obtained very quickly during freshwater injection.

4.2.3 Comparison of the two fluids injection

When the pressurized compressed air or freshwater (the applied pressure was greater than the groundwater pressure in the injection zone) was introduced into the soil layers, the vertical effective stress in adjacent regions decreased owing to the pore pressure increasing, the porosity in the corresponding zone increased, and the land uplift occurred due to the support action from the lower deformed soils. However, with the same applied pressure, the compressed air flowed to the ambient regions more quickly (in Fig. 8(a)) because of the difference between the air density and the groundwater density, whereas the freshwater spread to the surroundings relatively slowly (in Fig. 13) owing to the same density between the freshwater and groundwater. As a result, the influence range was greater for compressed air injection than for freshwater injection. Fig. 18 shows the distribution of changes in the vertical effective stress in the soil interior at 10.0 days for the two fluids injection. A negative value represented a decrease of vertical effective stress. The scope where the vertical effective stress decreased reached about 100 m horizontally during compressed air injection, whereas this scope only reached 20 m horizontally during freshwater injection. Moreover, the magnitude of changes in vertical effective stress was also significantly greater for compressed air injection than for freshwater injection. Similarly, the same was happening with the difference of porosity increment in the soil interior between these two fluids injection (in Figs. 10(b) and 15(b)).

Fig. 19 shows the time evolution of vertical displacement at the origin of ground surface

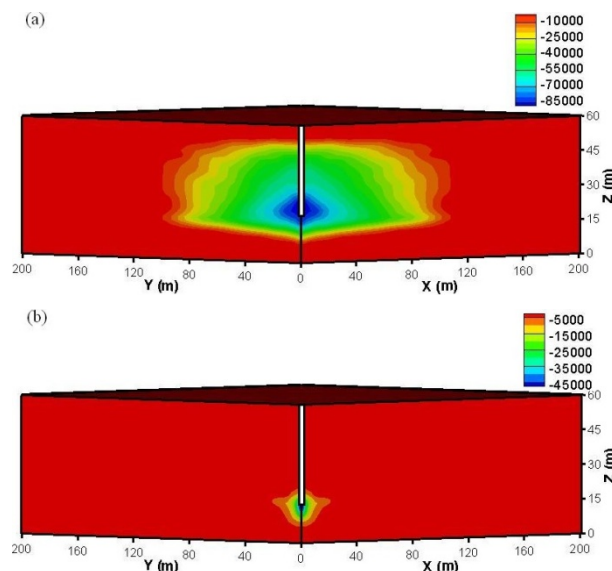


Fig. 18 The distribution of changes in the vertical effective stress in the soil interior at 10.0 days for: (a) compressed air injection; and (b) freshwater injection (unit: Pa)

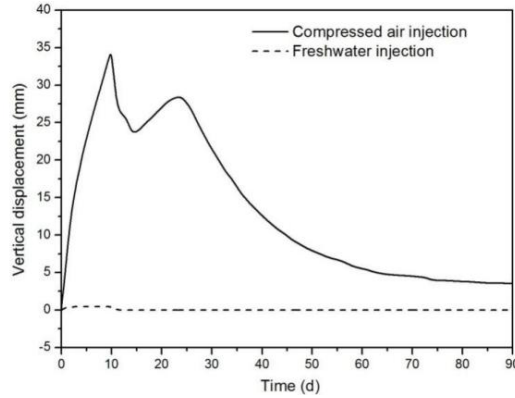


Fig. 19 The time evolution of vertical displacement at the origin of ground surface induced by the two fluids injection

induced by compressed air injection and freshwater injection. As can be seen, during fluids injection, the increase in surface vertical displacement for compressed air injection was much greater than that for freshwater injection, but this variation reached rapidly a quasi-steady state during freshwater injection. After fluids injection stopped, the surface vertical displacement for freshwater injection also decreased quickly to a very small value and remained unchanged, while this displacement for compressed air injection fluctuated continuously with time. From about 10 days to 15 days, the air in soil interior still flowed upwardly, and the airflow in the shallow soil layer dissipated rapidly, resulting in that the surface vertical displacement for compressed air injection decreased; While from 15 days to 25 days, the expansion of lower soil skeleton increased with the airflow in the deep soil layer moving upwardly, and the surface vertical displacement increased again; Hereafter, with the airflow dissipating, it decreased gradually and tended stable at 70.0 days. This phenomenon could be explained that the phase in the soil layer always remained single-phase liquid-saturated for freshwater injection, and it was easy to reach a balanced state. While the phase in the aquifer was transformed between a single-phase liquid-saturated state and a water-air two-phase state for compressed air injection, and it was difficult to obtain a quasi-steady state. In summary, the influence of compressed air injection on the geo-mechanical and water-air two-phase flow processes is greater, but this influence of freshwater injection reaches rapidly a quasi-steady state.

5. Conclusions

In this study, a loosely coupled liquid-gas-solid three-phase model, linking two numerical codes, TOUGH2/EOS3 and FLAC^{3D}, was established to investigate the interactions between the liquid phase, gas phase and solid phase in soils, then was validated using an in-situ air flow test in Essen. Hereafter, the coupled model was engaged to analyze the water-air two-phase flow processes and geo-mechanical processes induced by compressed air injection or freshwater injection in an aquifer of Tanggu District, Tianjin, China.

When the pressurized subsurface fluids is injected into the aquifer, the vertical effective stress in adjacent zones decreases due to the pore pressure here increasing, causing that the porosity increases and an expansion of soil skeleton appears in the corresponding zone. After the fluids

injection stops, both the magnitude and scope of porosity increments decrease and the soil deformation reduces. The land uplift is exactly caused by the support action from the lower deformed soils.

The main difference between compressed air injection and freshwater injection is that: Due to the difference in density between the compressed air and groundwater, the air spreads easily to the surroundings, and the effect of compressed air injection on the geo-mechanical and water-air two-phase flow processes is greater than that of freshwater injection at the same applied pressure; Additionally, the phase in the aquifer remains always a single-phase liquid-saturated state for freshwater injection, whereas it would be transformed between a single-phase liquid-saturated state and a water-air two-phase state for compressed air injection. Therefore, a quasi-steady state is obtained easily during and after freshwater injection, whereas the soil deformation develops continuously during compressed air injection, fluctuates with time due to the airflow moving upwardly after compressed air injection stops, and reaches a relatively stable value after a long time. Besides, during fluids injection, the air injection rate increases gradually with time, whereas the freshwater injection rate remains almost constant owing to a quasi-steady state. In conclusion, the effect of compressed air injection on the stress and seepage field is greater than that of freshwater injection, while all variables reach rapidly a quasi-steady state during and after freshwater injection. Especially, the land uplift caused by compressed air injection will not disappear immediately after the air injection stops. Therefore, for a water scarcity area, especially in Northern China, using compressed air injection instead of freshwater injection is a potion for controlling the land subsidence, and could be further studied in realistic fields and numerical simulation.

Acknowledgments

The research described in this paper was financially supported by the National Nature Science Foundation of China (Grant NO. 51579170 and 51179118) and the Science Fund for Creative Research Groups of the National Natural Science Foundation of China (Grant No. 51321065).

References

- Armero, F. and Simo, J.C. (1992), "A new unconditionally stable fractional step method for non-linear coupled thermomechanical problems", *Int. J. Numer. Methods Eng.*, **35**(4), 737-766.
- Bary, B. (2002), "Coupled hydro-mechanical and damage model for concrete as an unsaturated porous medium", *Proceedings of the 15th ASCS Engineering Mechanical Conference*, Columbia University, New York, NY, USA, June.
- Bell, J.W., Amelung, F., Ferretti, A., Bianchi, M. and Novali, F. (2008), "Permanent scatterer InSAR reveals seasonal and long-term aquifer-system response to groundwater pumping and artificial recharge", *Water Resour. Res.*, **44**(2), 282-288.
- Cappa, F., Rutqvist, J. and Yamamoto, K. (2009), "Modeling crustal deformation and rupture processes related to upwelling of deep CO₂-rich fluids during the 1965-1967 Matsushiro earthquake swarm in Japan", *J. Geophys. Res.*, **114**(B10).
- Chapuis, R.P. and Aubertin, M. (2003), "On the use of the Kozeny Carman equation to predict the hydraulic conductivity of soils", *Can. Geotech. J.*, **40**(3), 616-628.
- Chen, C.T., Hu, J.C., Lu, C.Y., Lee, J.C. and Chan, Y.C. (2007), "Thirty-year land elevation change from subsidence to uplift following the termination of groundwater pumping and its geological implications in

- the Metropolitan Taipei Basin, Northern Taiwan”, *Eng. Geol.*, **95**(1), 30-47.
- Chinkulkijniwat, A. (2005), “Multiphase flow in unsaturated soils and the induced deformation with respect to compressed air tunnelling”, Ph.D. Dissertation; Graz University of Technology, Austria.
- Chinkulkijniwat, A., Horpibulsuk, S. and Semprich, S. (2014), “Modeling of coupled mechanical–hydrological processes in compressed-air-assisted tunneling in unconsolidated sediments”, *Transport. Porous. Med.*, **108**(1), 105-129.
- Coussy, O. (1995), *Mechanics of Porous Continua*, Wiley, NY, USA.
- Dean, R.H., Gai, X., Stone, C.M. and Minkoff, S.E. (2006), “A comparison of techniques for coupling porous flow and geomechanics”, *SPE J.*, **11**(1), 132-140.
- Dror, I., Berkowitz, B. and Gorelick, S.M. (2004), “Effects of air injection on flow through porous media: observations and analyses of laboratory-scale processes”, *Water Resour. Res.*, **40**(9), 101-102.
- Felippa, C.A. and Park, K.C. (1980), “Staggered transient analysis procedures for coupled mechanical systems: formulation”, *Comput. Methods Appl. Mech. Engrg.*, **24**(1), 61-111.
- Gutierrez, M.S. and Lewis, R.W. (2002), “Coupling of fluid flow and deformation in underground formations”, *J. Eng. Mech.-ASCE*, **128**(7), 779-787.
- ITASCA Consulting Group Inc (2002), *Fast Lagrangian Analysis of Continua in 3 Dimensions Version 2.10; User’s Manual*. ITASCA Consulting Group Inc, MN, USA.
- Jeannin, L., Mainguy, M., Masson, R. and Vidal-Gilbert, S. (2007), “Accelerating the convergence of coupled geomechanical-reservoir simulations”, *Int. J. Numer. Anal. Methods Geomech.*, **31**(10), 1163-1181.
- Jha, B. and Juanes, R. (2007), “A locally conservative finite element framework for the simulation of coupled flow and reservoir geomechanics”, *Acta Geotech.*, **2**(3), 139-153.
- Kim, J. and Selvadurai, A.P.S. (2015), “Ground heave due to line injection sources”, *Geomech. Energy Environ.*, **2**, 1-14.
- Kim, J., Moridis, G., Yang, D. and Rutqvist, J. (2012), “Numerical studies on two-way coupled fluid flow and geomechanics in hydrate deposits”, *SPE J.*, **17**(2), 485-501.
- Kramer, J., and Semprich, S. (1989), “Erfahrungen über Druckluftverbrauch bei der Spritzbetonbauweise”, In: *Taschenbuch für den Tunnelbau, Deutsche Gesellschaft für Erd-und Grundbau*, Essen, Germany, pp. 91-153. [In German]
- Leverett, M.C. (1941), “Capillary behavior in porous solids”, *Trans. AIME*, **142**(1), 152-168.
- Lewis, R.W., Makurat, A. and Pao, W.K. (2003), “Fully coupled modeling of seabed subsidence and reservoir compaction of North Sea oil fields”, *Hydrogeol. J.*, **11**(1), 142-161.
- Minkoff, S.E., Stone, C.M., Bryant, S., Peszynska, M. and Wheeler, M.F. (2003), “Coupled fluid flow and geomechanical deformation modeling”, *J. Pet. Sci. Eng.*, **38**(1), 37-56.
- Mualem, Y. (1976), “A new model for predicting the hydraulic conductivity of unsaturated porous media”, *Water Resour. Res.*, **12**(3), 513-522.
- Öttl, G. (2003), *A Three-phase FE-model for Dewatering of Soils by Means of Compressed Air*, Universität Innsbruck AI, Publik.-Bereich.
- Pao, W.K. and Lewis, R.W. (2002), “Three-dimensional finite element simulation of three-phase flow in a deforming fissured reservoir”, *Comput. Methods Appl. Mech. Eng.*, **191**(23), 2631-2659.
- Pao, W.K., Lewis, R.W. and Masters, I. (2001), “A fully coupled hydro-thermo-poro-mechanical model for black oil reservoir simulation”, *Int. J. Numer. Anal. Methods Geomech.*, **25**(12), 1229-1256.
- Pruess, K., Oldenburg, C. and Moridis, G. (1999), *TOUGH2 User’s Guide Version 2.0*; University of California, Berkeley, CA, USA.
- Rao, D. (2001), “Gas injection EOR-A new meaning in the new millennium”, *J. Can. Petroleum Technol.*, **40**(2), 11-19.
- Rutqvist, J. (2008), *Analysis of injection-induced micro-earthquakes in a geothermal steam reservoir, the Geysers Geothermal Field*; Lawrence Berkeley National Laboratory, CA, USA.
- Rutqvist, J. (2012), “The geomechanics of CO₂ storage in deep sedimentary formations”, *Geotech. Gelo. Eng.*, **30**(3), 525-551.
- Rutqvist, J. and Tsang, C.F. (2003), “TOUGH-FLAC: A numerical simulator for analysis of coupled

- thermal-hydrologic-mechanical processes in fractured and porous geological media under multi-phase flow conditions”, *Proceedings of the TOUGH Symposium*, Berkeley, CA, USA, May, pp. 12-14.
- Rutqvist, J. and Moridis, G.J. (2007), “Numerical studies on the geomechanical stability of hydrate-bearing sediments”, *Proceedings of Offshore Technology Conference*, Houston, TX, USA, April-May.
- Rutqvist, J., Wu, Y.S., Tsang, C.F. and Bodvarsson, G. (2002), “A modeling approach for analysis of coupled multiphase fluid flow, heat transfer, and deformation in fractured porous rock”, *Int. J. of Rock Mech. Min. Sci., ITASCA Consulting Group Inc.*, **39**(4), 429-442.
- Rutqvist, J., Bäckström, A., Chijimatsu, M., Feng, X.T., Pan, P.Z., Hudson, J., Jing, L., Kobayashi, A., Koyama, T., Lee, H.-S., Huang, X.-H., Rinne, M. and Shen, B. (2009), “A multiple-code simulation study of the long-term EDZ evolution of geological nuclear waste repositories”, *Environ. Geol.*, **57**(6), 1313-1324.
- Rutqvist, J., Vasco, D.W. and Myer, L. (2010), “Coupled reservoir-geomechanical analysis of CO₂ injection and ground deformations at In Salah, Algeria”, *Int. J. Greenh. Gas. Con.*, **4**(2), 225-230.
- Samier, P., Onaisi, A. and de Gennaro, S. (2008), “A practical iterative scheme for coupling geomechanics with reservoir simulation”, *SPE Reserv. Eval. Eng.*, **11**(5), 892-901.
- Selvadurai, A.P.S. (2003), “Contaminant migration from an axisymmetric source in a porous medium”, *Water Resour. Res.*, **39**(8), 1204.
- Selvadurai, A.P.S. (2006), “Gravity-driven advective transport during deep geological disposal of contaminants”, *Geophys. Res. Lett.*, **33**(8).
- Selvadurai, A.P.S. (2009), “Heave of a surficial rock layer due to pressures generated by injected fluids”, *Geophys. Res. Lett.*, **36**(14).
- Settari, A. and Mourits, F.M. (1998), “A coupled reservoir and geomechanical simulation system”, *Soc. Pet. Eng. J.*, **3**(3), 219-226.
- Settari, A. and Sen, V. (2007), “The role of geomechanics in integrated reservoir modeling”, *The Leading Edge*, **26**(5), 622-627.
- Settari, A. and Walters, D.A. (2001), “Advances in coupled geomechanical and reservoir modeling with applications to reservoir compaction”, *Soc. Pet. Engrg. J.*, **6**(3), 334-342.
- Sreng, S., Li, L., Sugiyama, H., Kusaka, T. and Saitoh, M. (2009), “Upheaval phenomenon in clay ground induced by rising groundwater level”, *Proceedings of the 4th Biot Conference on Poromechanics*, Columbia University, NY, USA, June, pp. 106-203.
- Sun, D.M. and Semprich, S. (2013), “Using Compressed Air Injection to Control Seawater Intrusion in a Confined Coastal Aquifer”, *Transport. Porous. Med.*, **100**(2), 259-278.
- Teatini, P., Baú, D. and Gambolati, G. (2000), “Water-gas dynamics and coastal land subsidence over Chioggia Mare field, northern Adriatic Sea”, *Hydrogeol. J.*, **8**(5), 462-479.
- Teatini, P., Gambolati, G., Ferronato, M., Settari, A.T. and Walters, D. (2011), “Land uplift due to subsurface fluid injection”, *J. Geodyn.*, **51**(1), 1-16.
- Thomas, L.K., Chin, L.Y., Pierson, R.G. and Sylte, J.E. (2003), “Coupled Geomechanics and Reservoir Simulation”, *Soc. Pet. Eng. J.*, **8**(4), 350-358.
- Tsang, C.F., Birkholzer, J. and Rutqvist, J. (2008), “A comparative review of hydrologic issues involved in geologic storage of CO₂ and injection disposal of liquid waste”, *Environ. Geol.*, **54**(8), 1723-1737.
- Van Genuchten, M.T. (1980), “A closed-form equation for predicting the hydraulic conductivity of unsaturated soils”, *Soil Sci. Soc. Am. J.*, **44**(5), 892-898.
- Van Genuchten, M.T., Leij, F.J., Yates, S.R. (1991), *The RETC Code for Quantifying the Hydraulic Functions of Unsaturated Soils*; U.S. Salinity Lab., Riverside, CA, USA.
- Vijalapura, P.K., Strain, J. and Govindjee, S. (2005), “Fractional step methods for index-1 differential-algebraic equations”, *J. Comput. Phys.*, **203**(1), 305-320.
- Wong, R.C.K. and Lau, J. (2008), “Surface heave induced by steam stimulation in oil sand reservoirs”, *J. Can. Petrol. Technol.*, **47**(1), 13-17.